





RESEARCH ARTICLE

Development of myelination and axon diameter for fast and precise action potential conductance

Alisha L. Nabel^{1,2} | Laurin Teich^{1,2,3}  | Hilde Wohlfrom¹ | Olga Alexandrova¹ | Martin Heß⁴  | Michael Pecka¹  | Benedikt Grothe^{1,3} 

¹Division of Neurobiology, Faculty of Biology, Ludwig-Maximilians-Universität in Munich, Martinsried, Germany

²Graduate School of Systemic Neurosciences, Ludwig-Maximilians-Universität in Munich, Martinsried, Germany

³Division of Neurobiology, Faculty of Biology, Munich Cluster for Systems Neurology (SyNergy), Martinsried, Germany

⁴Division of Systematic Zoology, Faculty of Biology, Ludwig-Maximilians-Universität in Munich, Martinsried, Germany

Correspondence

Benedikt Grothe, Division of Neurobiology, Faculty of Biology, Ludwig-Maximilians-Universität in Munich, 82152 Planegg-Martinsried, Germany.
Email: grothe@lmu.de

Funding information

Deutsche Forschungsgemeinschaft, Grant/Award Numbers: Munich Cluster for Systems Neurology TPB7, SFB870 TPB2

Abstract

Axons of globular bushy cells in the cochlear nucleus convey hyper-accurate signals to the superior olivary complex, the initial site of binaural processing via comparably thick axons and the calyx of the Held synapse. Bushy cell fibers involved in hyper-accurate binaural processing of low-frequency sounds are known to have an unusual internode length-to-axon caliber ratio (L/d) correlating with higher conduction velocity and superior temporal precision of action potentials. How the L/d -ratio develops and what determines this unusual myelination pattern is unclear. Here we describe a gradual developmental transition from very simple to complex, mature nodes of Ranvier on globular bushy cell axons during a 2-week period starting at postnatal day P6/7. The molecular composition of nodes matured successively along the axons from somata to synaptic terminals with morphologically and molecularly mature nodes appearing almost exclusively after hearing onset. Internodal distances are initially coherent with the canonical L/d -ratio of ~ 100 . Several days after hearing onset, however, an over-proportional increase in axon caliber occurs in cells signaling low-frequency sounds which alters their L/d ratio to ~ 60 . Hence, oligodendrocytes initially myelinating axons according to their transient axon caliber but a subsequent differential axon thickening after hearing onset results in the unusual myelination pattern.

KEYWORDS

axon diameter, globular bushy cell, internode, myelination, Node of Ranvier

1 | INTRODUCTION

Myelination patterns play a vital role in determining the conduction, shape, propagation velocity, and temporal precision of action potentials,

all of which are key features of neuronal processing (Hursh, 1939; Seidl, 2014; Mathis & Vallat, 2019). Thus, conduction velocity (CV) in myelinated axons crucially depends on axonal diameter, myelin thickness, the lengths of individual myelin sheaths, also referred to as internodes, and nodal length itself (Arancibia-Cárcamo et al., 2017; Huxley & Stampfli, 1949; Smith & Koles, 1970; Waxman, 1980). The

Alisha L. Nabel and Laurin Teich contributed equally to this work.

This is an open access article under the terms of the [Creative Commons Attribution-NonCommercial-NoDerivs](https://creativecommons.org/licenses/by-nc-nd/4.0/) License, which permits use and distribution in any medium, provided the original work is properly cited, the use is non-commercial and no modifications or adaptations are made.

© 2024 The Authors. GLIA published by Wiley Periodicals LLC.

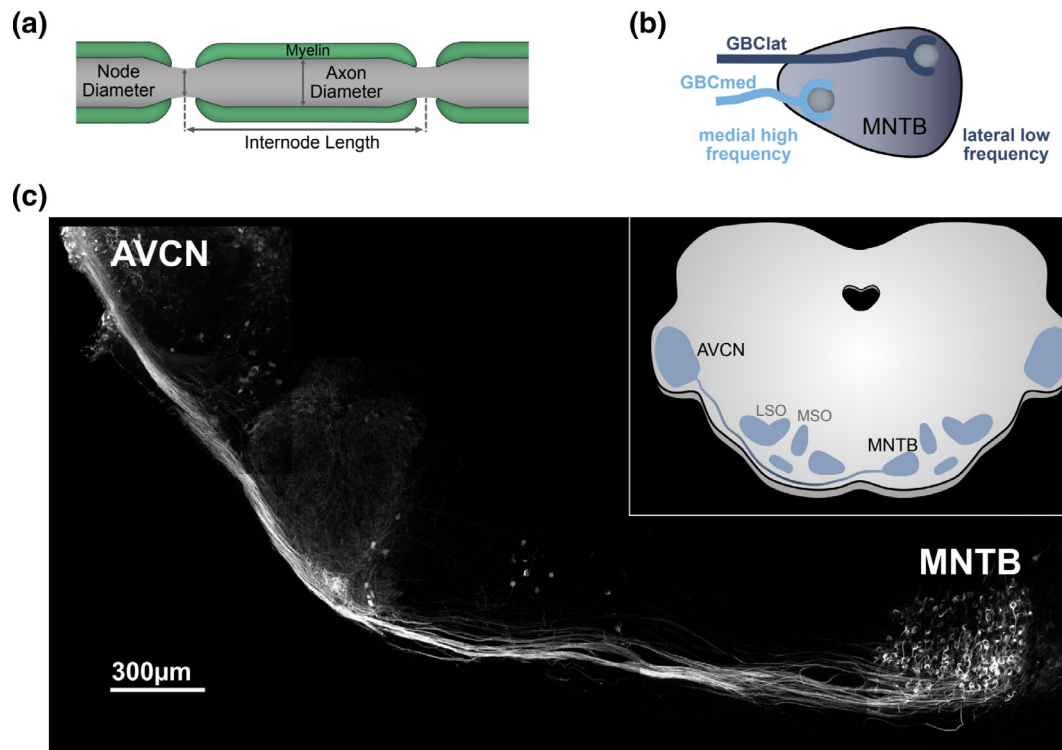


FIGURE 1 GBC Axons in the AVCN to MNTB Connections. (a) Scheme of a myelinated axon with definitions of the parameters analyzed. (b) The tonotopically organized MNTB. (c) Confocal image (maximum projection of several optical sections) of a coronal section of the brainstem at P8. Cell bodies of biocytin-labeled GBC axons originate in the AVCN and terminate on principal cells of the MNTB. The inset shows a scheme of the pathway (AVCN, anterior ventral cochlear nucleus; MNTB, medial nucleus of the trapezoid body; MSO, medial superior olive; LSO, lateral superior olive). Scale bar: 300 μm .

ratio of internode length-to-axon diameter (L/d ratio) (Figure 1a) has been shown to play a key role in setting the CV (Ford et al., 2015).

Despite its functional significance for almost all neuronal circuits in the brains of higher vertebrates, it is still unclear how specific myelination patterns are established and whether axons or oligodendrocytes (the myelinating cells) define the L/d ratio (Bechler et al., 2015; Bechler et al., 2017).

Generally speaking, internode length scales positively with axon diameter, and most axons measured throughout the vertebrate nervous system have an L/d ratio of around 100 (Hursh, 1939; Rushton, 1951; Waxman, 1980). This relation has been shown, for example, in the peroneal nerve (PNS) of kittens and adult cats. There are, however, significant exceptions to this rule, which may shed light on the question of how the L/d ratio is modulated. In the Mongolian gerbil (*Meriones unguiculatus*), a subset of globular bushy cell (GBC) axons, which are essential components of the mammalian sound localization circuit, exhibit for example such an unusual myelination pattern. Mongolian gerbils have unusual good low-frequency hearing and exploit minute differences in the time of arrival of low-frequency sounds at the two ears, so-called interaural time differences (ITD; note that interaural level differences are absent for low-frequency sounds only). Behavioral tests showed a resolution of about 20 μs , almost identical to that of humans (Lesica et al., 2010; Tolnai et al., 2017). Most other rodents, like mice, do not hear such low frequencies and

do not need to exploit ITDs (Grothe & Pecka, 2014). The Mongolian gerbil, however, has a hearing range similar to us humans. In gerbils, but not in the only high-frequency-hearing mice (Stange-Marten et al., 2017), GBC axons terminating in the lateral third nucleus of the trapezoid body (MNTB) are known to be tuned to low sound frequencies (<2 kHz) and constitute a crucial component of the ITD processing circuit (Brand et al., 2002; Grothe & Pecka, 2014). These fibers are of comparably large axon caliber but exhibit unexpectedly short internodes resulting in unusually low L/d ratios of <60. Theoretical considerations indicate that, for a given axon caliber, shorter internodes result in faster action potential rise-time, shorter half width, and larger amplitude, which, together, should increase CV, although at comparably large costs (Ford et al., 2015). In fact, measurements of CV in vitro and in vivo confirmed that conduction velocity and action potential precision are significantly higher in GBCs with thicker axon caliber compared to thinner GBCs with similar internodal length. The latter GBCs are tuned to higher sound frequencies, appear ordinary in myelin configuration and physiology (Ford et al., 2015), and are similar to all GBC axons in mice, which do not hear low sound frequencies (Stange-Marten et al., 2017). Comparable measurements do not exist for other mammals (including humans), but other physiological and structural specializations in this neural circuit related to hyperprecise processing of low-frequency-sound-derived signals have been described across different orders of mammals (Grothe, 2003;

Mansour & Kulesza, 2021). Therefore, it seems unlikely that the axon-related specializations are limited to low-frequency hearing rodents.

We have studied the development of the GBC axons and their myelination schedule in the gerbil. The initial myelination and node formation started around day postnatal 7 (P7) continuing until about a week after hearing onset. Nodes developed sequentially along the axon with nodes near the somata maturing first, and nodes close to the axonal terminal maturing latest. Initially, L/d ratios were similar in all GBC axons close to the canonical value of around 100. Only after hearing onset, and in parallel with the completion of node development the caliber of GBC axons increase differentially. This was most evident in low-frequency GBC axons, which accounts for their unusually low L/d ratio.

2 | RESULTS

In the adult Mongolian gerbil, the L/d ratio differs significantly between GBCs tuned to low sound frequencies and terminating in the lateral part of the MNTB ($L/d \sim 60$) compared to medially terminating GBCs that are tuned to mid and high sound frequencies ($L/d \sim 100$). In order to assess whether this difference occurs right from the early stages of myelination or only later during development, we evaluated the development of myelination, of Nodes of Ranvier, and of axon caliber in GBC axons in Mongolian gerbils (*M. unguiculatus*; Figure 1a). GBC somata are located in the ventral cochlear nucleus. Each GBC axon projects to the contralateral MNTB where it synapses on one MNTB principal neuron via a Calyx of Held (Friauf & Ostwald, 1988; Figure 1b). We visualized axons and Nodes of Ranvier by intracellularly filling GBCs with biocytin combined with immunohistochemical labeling of nodal (AnkG), paranodal (CASPR), and juxtaparanodal (Kv1.2) markers (Figure 1c). By following single labeled axons and determining their termination in a calyx of Held within the MNTB, we distinguished low-frequency fibers (lateral 1/3 of the MNTB) from high-frequency fibers (medial 1/3 of the MNTB; Figure 1b). This is possible since the monosynaptic connection of GBC fibers to MNTB neurons via the Calyx of Held synapses follows a strict tonotopic arrangement from lateral (tuned to low frequencies) to medial positions (tuned to high sound frequencies (compare: Ford et al., 2015; Stange-Marten et al., 2017)).

2.1 | First signs of myelination in the superior olivary complex in the first postnatal week while myelination is completed around hearing onset (P13)

To define the relevant developmental time frame we investigated the development of myelin in the superior olivary complex by immunolabeling coronal gerbil brainstem sections and sagittal sections of the trapezoid body (TB) at different developmental time points (Figures 2 and S2), the fiber bundle consisting of GBC axons to MNTB (overview of the superior olivary complex see Figure S1). We used antibodies against the neurofilament heavy (NFH) and the neurofilament-

associated antigen (3A10) as axonal markers. Both axonal marker antibodies were found to show a similar staining result in the gerbil auditory brainstem. Antibodies against the myelin basic protein (MBP) were used to demonstrate myelin. We could identify the first signs of myelination in the superior olivary complex at the end of the first postnatal week (Figures 2a,d, and S1A and S2). However, in sagittal sections at postnatal day 7, the majority of TB fibers are still not myelinated (Figure 2d). Two days later, at postnatal day 9 most fibers are fully myelinated and only single unmyelinated fibers can be detected (arrow) (Figure 2b). In line with that, in sagittal slices at postnatal day 10, most fibers are surrounded by myelin (Figure 2e). At postnatal day 13, all axons are fully covered with myelin sheaths (Figures 2c and S1C). Consistent with the latter finding sagittal sections of postnatal day 14 exhibit all axons to be myelinated (Figure 2f). Hence, the first indications of nodes and myelination appear at around P6/7, about 5–6 days before hearing onset. By P13 coverage with myelin sheaths along the entire axon was essentially completed. Therefore, we compared the development of axonal and myelination morphology and of the Node of Ranvier in detail from P6/P7 up to >P49 (adult).

2.2 | Nodes of Ranvier appear days before the onset of hearing but continue to mature for another week

In more detail, we then investigated the appearance and development of nodes by determining their molecular composition throughout their postnatal development. Therefore, we immunolabeled the nodal scaffolding protein ankyrin G (AnkG), the paranodal adhesion molecule contactin-associated protein 1 (CASPR), and the juxtaparanodal (delayed rectifier) voltage-gated potassium channel $K_v1.2$ in brainstem sections with biocytin-filled GBC fibers of gerbils at P6/P7 (the earliest stage at which we could identify developing nodes), P8 (partial myelination), P12 (around hearing onset), P15 (3 days after hearing onset), P26 (an age at which most auditory brainstem structures are adult-like (Kandler et al., 2009) and around P50 (P49/50/51; fully mature stage). We imaged segments of the axon using a high resolution in order to capture the Nodes of Ranvier. The imaging data, however, does not cover the entire length of the axon which would be needed to faithfully trace medial and lateral GBC axons along their entire projection path. Therefore, we did not distinguish lateral and medial GBC axons for the detailed description of node development. Although AnkG, CASPR, and $K_v1.2$ are characteristic for distinct compartments of the Nodes of Ranvier in adults (P26, P50), at the earlier developmental stages (P6/P7 to P15) we observed a considerable degree of colocalization of these proteins (Figures 3 and S2). Clusters of CASPR (green), in association with more diffuse zones of AnkG (red), first appeared on P6/P7 (Figure 3b, top). During the second postnatal week (P8–P15), several distinct patterns of CASPR and AnkG clusters were detected (see below), whereas at P26 and ~P50 fully mature nodes strongly predominate (Figure 3b, bottom).

Figure 3a depicts the color code used for the identified patterns of immunostaining (node categories) shown in Figure 3b (left). Areas

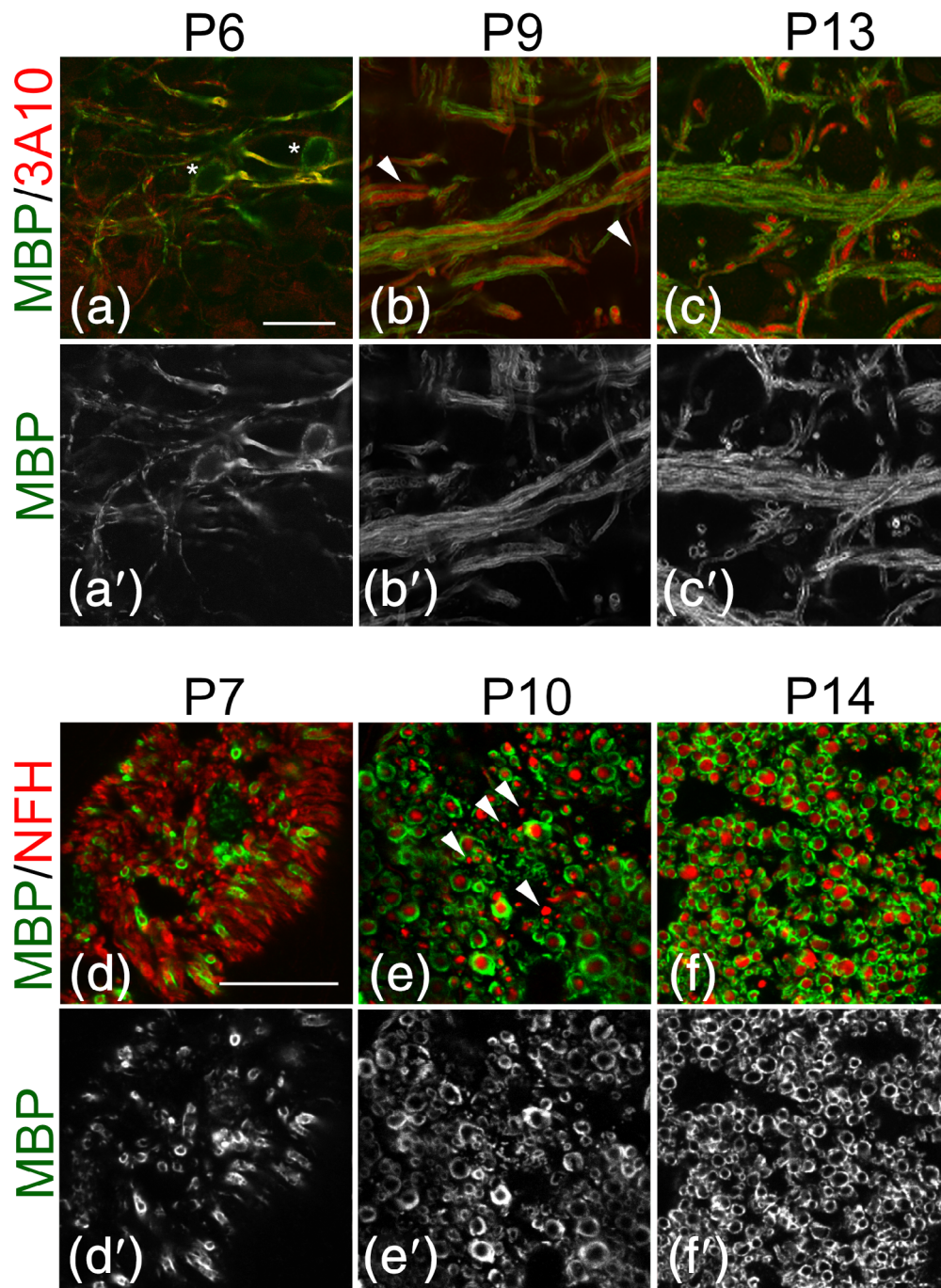


FIGURE 2 High-resolution images of myelin in trapezoid body (TB) of the Mongolian gerbil. Antibodies against neurofilament-associated antigen (3A10) (a–c) and neurofilament heavy (NFH) (d–f) are used as axonal markers. Antibodies directed against myelin basic protein (MBP) demonstrate myelin. Confocal single optical images were acquired from coronal vibratome sections of the gerbil brain in TB area at postnatal day 6 (a, a'), postnatal day 9 (b, b') and postnatal day 13 (c, c'). Confocal single optical sections were acquired from sagittal vibratome sections of the gerbil brain in the TB area at postnatal day 7 (d, d'), postnatal day 10 (e, e') and postnatal day 14 (f, f'). (a–f) Axonal markers 3A10 (a–c) and NFH (d–f) shown in red, MBP immunoreactivity depicted in green. (a'–f') The corresponding images of MBP staining. At postnatal day 6 (a, a') short, sometimes punctate, fragments of myelin, interspersed with long non myelinated gaps are visible. Oligodendrocytes (white asterisks) actively producing MBP, are brightly labeled with anti MBP antibodies. In sagittal sections at postnatal day 7, cross section of TB fibers are visible. A small proportion of TB axons are surrounded by MBP, labeled with anti MBP antibodies. At postnatal day 9 (b, b') the most part of the axons in TB is myelinated. However, one can easily notice that some axons are not wrapped by the myelin (white arrowheads, b). In sagittal sections at postnatal day 10, most axons are wrapped by myelin while some are not (white arrowheads, e). By postnatal day 13 (c, c') myelin sheath can be seen around all axons. Note that myelinated axons are lying so tightly, that it is difficult to outline myelin sheath belonging to the single axon. In sagittal sections at postnatal day 14, all axonal cross sections in the TB area are surrounded by myelin. Scale bar: 20 μ m.

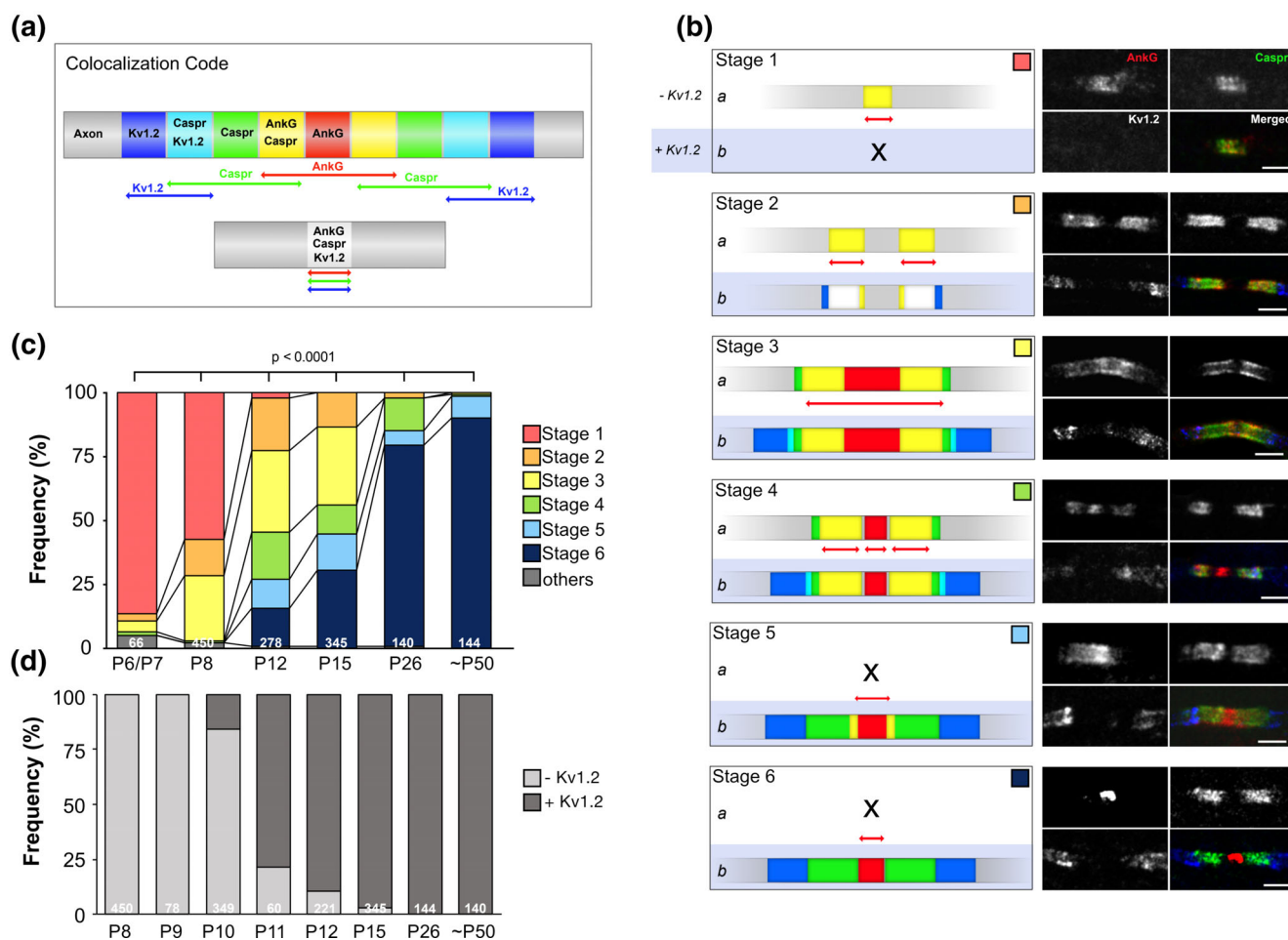


FIGURE 3 Developmental clustering of nodal, paranodal and juxtaparanodal components along GBC axons. GBC axons were immunostained with antibodies specific for the nodal marker AnkG (red), the paranodal marker CASPR (green) and the juxtaparanodal marker $K_v1.2$ (blue). (a) Colocalization code for AnkG, CASPR and $K_v1.2$ clusters. Colors correspond to the additive RGB color model. Non-colocalized immunostaining of AnkG, CASPR and $K_v1.2$ are depicted in red, green, and blue, respectively. Overlap of AnkG and CASPR results in yellow, co-expression of CASPR and $K_v1.2$ appears as turquoise. All three colors together result in white. (b) Scheme (left) of different stages of node formation from 1 to 6. Representative images of the corresponding category are shown in the right panel. Scale bars: 2.5 μm . The development of nodes of Ranvier proceeds from Stage 1 to 6, as demonstrated below (see c and text). X indicates that either no nodes were found with $K_v1.2$ clusters (Stage 1) or no nodes were found without $K_v1.2$ clusters (Stage 5 & 6). The description of the colocalization code used in Stage 1–6 is shown in Figure 3a. (c) Quantitative analysis of each category of nodal stage at different ages. Numbers on bars are numbers of analyzed nodes. Numbers of animals: P6/P7: three, P8: four; P12: five; P15: four, P26: four, P49–P51 (~P50): three. P-values are derived from χ^2 tests. (d) Expression of $K_v1.2$ at nodes of Ranvier during development. $K_v1.2$ is detectable starting from P10. The percentage of nodes immunolabeled for $K_v1.2$ increases starting from P11. Numbers on the bars represent the number of nodal clusters analyzed.

solely stained for AnkG, CASPR, and $K_v1.2$ are shown in red, green, and blue, respectively. Overlapping of AnkG and CASPR is depicted in yellow, and the colocalization of CASPR and $K_v1.2$ is represented in turquoise. Colocalization of all three markers is shown in white. To classify the identified nodes into different developmental stages, we measured the lengths of the CASPR and AnkG clusters and quantified the degree of overlap. Based on this, we were able to distinguish six categories of nodes. (1) A “Stage 1” pattern of overlapping AnkG and CASPR. (2) A “Stage 2” pattern consisting of two adjacent “Stage 1” clusters. (3) A “Stage 3” cluster composed of a central AnkG expression zone and two bordering paranodal CASPR clusters, in which the broad AnkG clusters continued into the paranodal regions and fully or partly overlapped with CASPR. (4) A “Stage 4” expression pattern

with a focal AnkG zone and two adjacent clusters overlapping with CASPR. Sometimes the lateral and focal parts exhibited different intensities. (5) A “Stage 5” pattern consisting of a narrow AnkG cluster in the center with two adjacent paranodal CASPR clusters, but with a small overlap between AnkG and CASPR. (6) The “Stage 6” is the last category, which corresponds to the well-known mature configuration. Stage 6 is characterized by a focal AnkG cluster in the nodal region with two flanking CASPR clusters at the paranodes. In this category, AnkG and CASPR clusters never overlapped.

At P6/P7 (66 nodes/3 animals), the vast majority of nodes (86.4%) showed immature clusters of AnkG and CASPR (Cat.1). At P8 (450 nodes/4 animals), this is still the most frequent class (57.8%), while 13.8% of nodes belonged to Cat. 2, and 25.8% to Cat. 3. Clusters

assigned to Cat. 4 accounted for only 0.7% of nodes, and no examples of Cat.5 or Cat. 6 were found in animals of this age. A low number of nodes (2%) could not be categorized and were classified as “other” (Figure 3c). At P12 (around the onset of hearing; 278 nodes/5 animals), the incidence of Cat. 1 nodes decreased sharply to only 2.2%, whereas categories 2 (20.5%), 3 (31.6%) and 4 (19.1%) were most frequent. At this age, a few Cat. 5 (11.2%) and Cat. 6 (14.8%) nodes were also present.

No Cat. 1 nodes were found at P15 (345 nodes/4 animals), and only 13% belonged to Cat. 2. The most frequent clusters were now of categories 3 (30.7%) and 6 (30.3%), while 11.3% of nodes belonged to Cat. 4 and 14.8% to Cat. 5. In young adults, at P26 (140 nodes/4 animals), the more immature clusters (Cat. 1–3) were almost entirely absent. However, Cat. 4 (12.9%) and Cat. 5 (5.7%) nodes were still identifiable at this age, although the majority of nodes (78.6%) were assigned to Cat. 6. At ~P50 (P49-P53; 144 nodes/3 animals), 90.3% of nodes were classified as Cat. 6, and 8.3% as Cat.5. Less mature nodes were barely detectable.

The voltage-gated potassium channel $K_v1.2$ appeared to localize to nodes independently of the developmental categories we identified (Figure 3d), with the exception of Cat. 1, in which it was never observed. Thus, $K_v1.2$ is not expressed in the Nodes of Ranvier at P8 and P9 and was expressed in only 15.7% of nodes at P10. At P11

(78%) and P12 (89%), large proportions of nodes were $K_v1.2$ immunopositive. At P15, almost all nodes (98%) showed $K_v1.2$ expression. Interestingly, in both P12 and P15, we found nodes of categories 2, 3, and 4 with and without $K_v1.2$. However, $K_v1.2$ was not always restricted to the juxtaparanodal region but extended into the paranodal region and often showed an asymmetric distribution by P15. At P26 and later, $K_v1.2$ was expressed in all juxtaparanodal regions of the identified nodes.

These data show that morphologically and molecularly mature nodes appear almost exclusively after hearing onset.

2.3 | Nodes of Ranvier develop sequentially according to their location along GBC axons

The distribution of nodal developmental categories did not occur uniformly or randomly along the axon, but rather in a specific regional sequence, as visible via dividing the axonal tract that runs from the AVCN (GBC somata) toward the calyx of Held in the contralateral MNTB into three distinct areas (Figure 4; for more details and cluster separation see Figure S3). Area A extends from close to the AVCN/somata to the ipsilateral LSO, B from adjacent to the ipsilateral MSO to the midline (B), and C from close to the contralateral MNTB to the

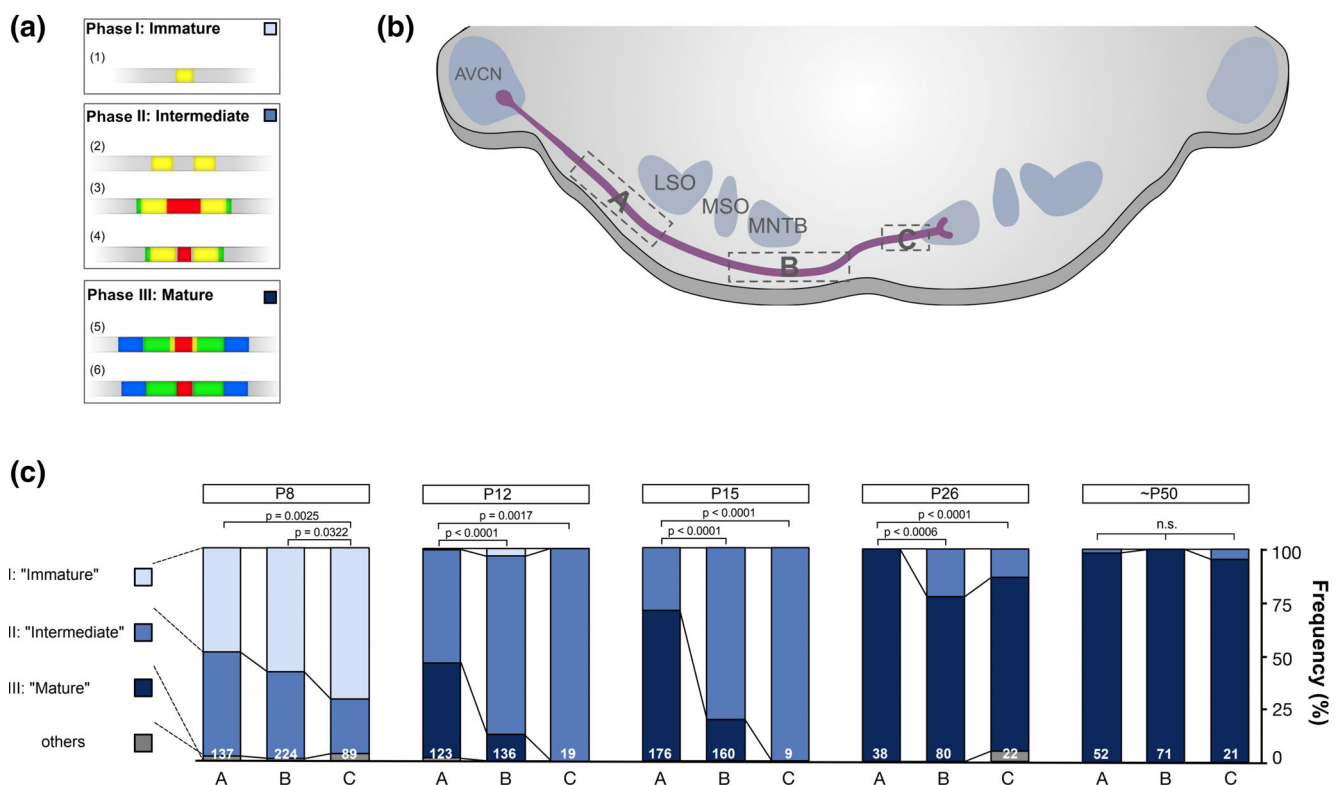


FIGURE 4 Development of nodal clusters in distinct regions along the AVCN-MNTB tract. (a) The nodal categories in Figure 3 were reduced to three developmental phases. Cat. 1 is classified as immature phase I; Cat. 4 corresponds to immature phase II; and Cat. 5 and Cat. 6 are mature phase III nodes. (b) Scheme of the auditory brainstem including the AVCN-MNTB with analyzed regions boxed. AVCN – iLSO (ipsilateral LSO, a), iMSO-midline (b), cMNTB (contralateral MNTB, c). (c) Quantification of nodal stages according to their location at P8, P12, P15, P26 and ~P50. Numbers on the bars represent the number of nodal clusters analyzed. *p* Values are derived from χ^2 tests.

calyx of Held. We reduced the previous six nodal categories (see Figure 3) to three developmental phases (Figure 4a): immature ("Stage 1"), intermediate ("Stages 2–4") and mature ("Stages 5 and 6"). At P8–P15 we found a clear differential distribution of nodal categories, with the more developed nodes lying closer to the somata and the less mature nodes closer to the synaptic terminal (calyx of Held; for details, see Figure 6c). For instance, at P8 the proportions of immature "phase I" (48.9%) and intermediate "phase II" (48.91%) nodes in area A clearly differed from those found in area C, which is most remote from the somata ("phase I": 70.8%, "phase II": 25.8%; $p = .0025$, χ^2 test). At P12, mature "phase III" accounted for half (44.7%) of the nodes in area A, while in area C all analyzed nodes were classified as intermediate "phase II" ($p = .0017$). We observed the same trend after the onset of hearing: At P15, 70.5% of the nodes in area A were classified as "phase III" (mature), while in areas B (80%; with respect to A: $p < .000$, χ^2 -test) and C (100%; with respect to A: $p < .0001$, χ^2 -test) nodes were almost exclusively in "phase II" (intermediate). In young adults (P26) and adults (~P50), the majority of nodes were "phase III" (mature) with only few or no regional differences.

2.4 | Internode length is established before the onset of hearing and is similar in laterally and medially ending GBC fibers

We then quantified the internode length of either laterally (GBClat) or medially (GBCmed) terminating fibers in animals at P10/P15 (young animals), time points around the onset of hearing. We analyzed the internode length for P10 and P15 individually, but having observed no significant differences between these ages for GBClat and GBCmed, we did not discriminate between these age groups and pooled the data, before comparing them to the data for young adults (P25). The data from the young adult (P25) age group used in this study are re-analyzed and replotted from (Ford et al., 2015) (identical methods).

We found that within the last 500 μm before the synaptic terminal, the mean internode length at P10/P15 decreased consistently toward the calyx of the Held terminal in both GBClat and GBCmed fibers (Figure 5a), as also seen in P25 animals (Ford et al., 2015). The mean internode length in GBClat fibers decreased progressively by more than half from $181.2 \pm 13.42 \mu\text{m}$ (seventh internode from calyx; $n = 15$ internodes) to $78.74 \pm 13.08 \mu\text{m}$ (last internode before calyx; $n = 18$, $p < .0001$, Mann–Whitney U test; Figure 5b). Similarly, in GBCmed fibers of young animals, the internode length decreased by as much as 75%, from $226.7 \pm 25.15 \mu\text{m}$ (seventh internode from calyx; $n = 9$ internodes) to $55.42 \pm 16.30 \mu\text{m}$ (last internode before calyx; $n = 15$, $p < .0001$, Mann–Whitney U test).

However, internode lengths at least a few hundred micrometers from the calyx is uniform ("steady-state area" (<500 μm from the calyx, compare Ford et al., 2015; Figure 5c) of GBClat, did not differ significantly between young animals ($190.8 \pm 8.54 \mu\text{m}$; $n = 18$ axons/7 animals) and young adults for GBClat ($210.2 \pm 12 \mu\text{m}$, $n = 9$ axons/3 animals; $p = .2$, Student's t -test) nor for GBCmed (P10/15: $205.9 \pm 9.86 \mu\text{m}$, $n = 15$ axons /11 animals; P25: $241.2 \pm 17.43 \mu\text{m}$,

$n = 8$ axons/2 animals; $p = .07$, Student's t -test). Moreover, internode length far from calyx did not statistically differ between GBClat and GBCmed either at P10/15 ($p = .2519$, Student's t -test) or at P25 ($p = .1564$, Student's t -test; for the steady state area, a total of 114 measurements were taken from lateral axons of p10, p15, and p25 animals; a total of 86 measurements were taken from medial axons of p10, p15, and p25 animals). This indicates that the internodal length is determined during myelination, which occurs before hearing onset.

2.5 | The larger diameter of the laterally ending GBC axons only develops several days after the onset of hearing

To further assess the development of the relevant structural parameters of GBC axons, we next determined the diameters of the Nodes of Ranvier and compared animals on P10/P15, to young adults on P25 (Figure 6a) of both the GBClat and GBCmed. As for the internode length, we also merged the data of P10 and P15 for the nodal diameter. We found that the mean nodal diameter of GBClat in young animals (P10/15: $1.27 \pm 0.07 \mu\text{m}$, $n = 18$ axons/7 animals) at around hearing onset had increased significantly by P25 ($1.9 \pm 0.06 \mu\text{m}$; $n = 8/2$; $p < .0001$, Mann–Whitney U test). Likewise, the nodal diameter of GBCmed increased from $1.25 \pm 0.07 \mu\text{m}$ ($n = 15$ axons/11 animals) at P10/P15 to $1.56 \pm 0.12 \mu\text{m}$ ($n = 8$ axons/2 animals) at P25 ($p = .0254$; Student's t -test). Hence, while nodal diameter did not differ between GBClat and GBCmed at P10/15 ($p = .9501$, Mann–Whitney U test), a clear difference becomes apparent by P25 ($p = .0159$, Student's t -test).

As in the case of P25 animals (see Ford et al., 2015), in P10/P15 animals, node diameter also increases in the direction of the calyx of Held (Figure 6b). The mean nodal diameter of GBClat fibers increased by 28.57% from $1.19 \pm 0.09 \mu\text{m}$ at the 5th node before heminode) to $1.53 \pm 0.12 \mu\text{m}$ at the last node before heminode ($p = .029$, Student's t -test; total number of nodes 15) and by 30.36% in GBCmed—from $1.12 \pm 0.12 \mu\text{m}$ (fifth node before heminode) to $1.46 \pm 0.15 \mu\text{m}$ (last node before heminode; $p = .0453$, Mann–Whitney U test; $n = 15$).

Since not only the Nodes of Ranvier and the internode length but rather the ratio of internodal length to axon caliber, has an essential impact on action potential shape and conduction velocity (see Ford et al., 2015), we examined the axon diameter of GBClat and GBCmed at different developmental stages.

Figure 6c shows representative confocal images of immunohistochemically labeled GBC axons at P10 (left) and P25 (right). Even on sight, the axon caliber appears much smaller at P10 than at P25 (Figure 6c, top; for quantification, see next section). We also observed a marked increase in the inner axon diameter upon comparing the P10 and P25 sections obtained by transmission electron microscopy (TEM; Figure 6c, bottom). We calculated axon diameters in TEM images from measurements of the circumferences of individual axons (without their myelin sheaths). Despite their methodological differences, the range and minima and maxima of measured axon diameter

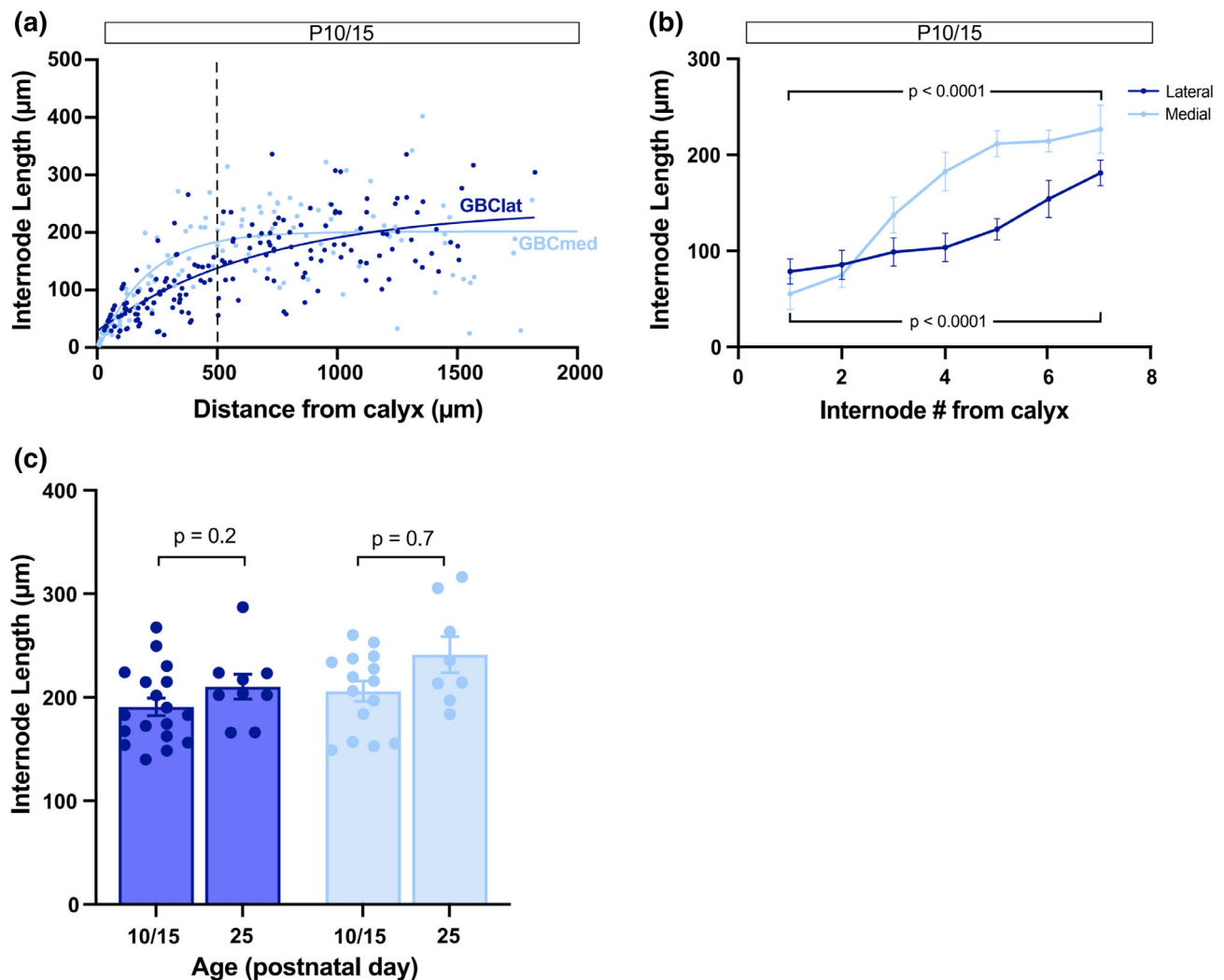


FIGURE 5 Internode length of GBC fibers remains virtually constant throughout development. (a) Internode length plotted against the distance from the heminode in young animals (P10/15). Each data point represents a single internode length of all analyzed axons, and the x-value displays the position of the intermodal center. The vertical dashed line indicates the beginning of the steady-state section of internode length. (b) Internode length plotted as a function of internode number from calyx at P10/15. Data are presented as mean \pm SEM. The mean internode length in young animals decreases from the 7th internode from the calyx to the internode closest to the calyx in GBCmed and GBClat fibers ($p < .0001$, Mann–Whitney *U*-test). (c) Mean internode length in GBClat and GBCmed fibers in young animals (P10/15) and young adults (P25). Only values from the steady-state section $>500 \mu\text{m}$ (for P10/15) and $>700 \mu\text{m}$ (P25) from calyx were used. Data are presented as mean \pm SEM and every data point represent the average internode length of a single axon. *p* Values are derived from student's *t*-test.

at P10 obtained by the TEM and IHC approaches were comparable (data not shown). Together with earlier validations of the method (Ford et al., 2015; Sinclair et al., 2017), these results led us to retain the IHC approach in subsequent experiments.

Using this strategy, we were able to determine axon calibers of GBClat and GBCmed at different developmental stages on P8 (shortly after the onset of myelination), P10 (about 3 days before hearing onset but already with consistent evidence for Nodes of Ranvier), P15 (3 days after hearing onset), P17 (at which time structural and functional refinements in the auditory brainstem are known to be highly dynamic (Magnusson et al., 2005), P25 (an age at which most auditory brainstem structures are adult-like; (Kandler et al., 2009), and around P50 (P49/P53) as a mature stage. Since

our approach required the tracing and reconstruction of GBC axons with a length of approximately 1 mm in a complex 3D structure, the number of reconstructed axons is limited but yielded sufficient numbers of measured points (with at least two GBCmed axons and two GBClat axons from at least two different animals in each age group).

Figure 6d shows the internodal axon diameter at different ages (postnatal days) for GBClat (dark blue) and GBCmed (light blue). Each data point represents the mean of the internodal axon diameter of an individual axon, assessed by averaging numerous internodal measurements along the reconstructed axon. For each individual internode, 5–10 independent measurements were obtained, and 7–12 internodes were quantified from every axon.

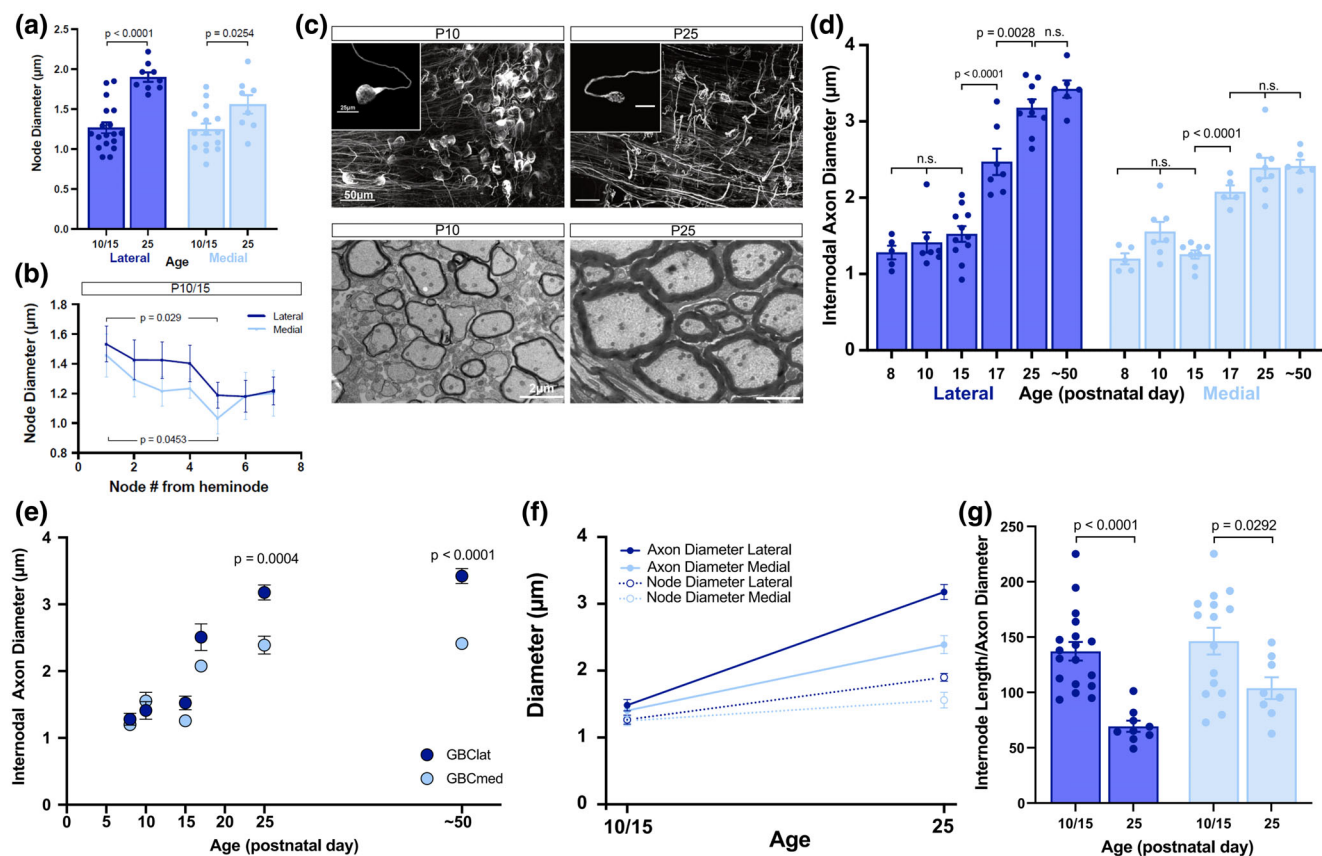


FIGURE 6 The internodal axon diameter of laterally ending GBCs grows differentially after hearing onset. (a) The average diameter of nodes of Ranvier on GBC axons increases from P10/15 (young animals) to P25 (young adults). (b) Nodal diameter plotted as a function of node number starting from heminode at P10/15. In young animals (P10/15), the mean diameter of nodes of Ranvier on GBCLat and GBCMed fibers increases from the 5th node from heminode to the first node from heminode. Data are presented as mean \pm SEM and P-values derive from Student's *t*-test or the Mann–Whitney *U* test, depending on the distribution of the data. (c) Representative image (maximum projection of several optical sections) of biocytin-filled GBC axons (top) innervating the MNTB at P10 (left) and P25 (right). Scale bars: 50 μ m. Insets show magnifications of single digitally extracted GBCLat. Scale bars: 25 μ m. Transmission electron micrograph (bottom) of parasagittal section through the GBC fiber tract at P10 (left) and P25 (right). Scale bar: 2 μ m. (d) The average internodal axon diameter of GBCLat and GBCMed increased from P8 to P50. P-values are derived from one-way ANOVA with Bonferroni's post-hoc test. Each data point in represents the mean of a single axon. (e) Comparison of the internodal axon diameter between GBCLat and GBCMed during postnatal development. P-values are derived from Student's *t*-test. (f) Axonal (solid line) and nodal (dashed line) diameters are similar at P10/15. Axon diameter later increases dramatically, whereas node diameter does so only moderately. (g) The mean internode length to axon diameter (*L/d*) ratio in GBCLat and GBCMed fibers in young animals (P10/15) and young adults (P25). Only values from the steady-state section >500 μ m (for P10/15) and >700 μ m (P25) from calyx were used. Data are presented as mean \pm SEM and every data point represent the *L/d* ratio of a single axon. *p* Values are derived from student's *t*-test.

The average internodal axon diameter of GBCLat (Figure 6d, dark blue) at P8 was 1.28 ± 0.09 μ m (mean \pm SEM; $n = 5$ axons/2 animals) and had increased only slightly (statistically not significant) by P10 (1.41 ± 0.13 μ m, $n = 7/2$; $p > .9999$, one-way ANOVA with Bonferroni's post-hoc test) and from P10 to P15 (1.52 ± 0.10 μ m; $n = 11$ axons/4 animals; $p > .9999$). However, at P17, only 2 days later, the axon caliber of GBCLat was significantly larger (2.51 ± 1.20 μ m, $n = 6$ axons/2 animals; $p < .0001$) and increased further until P25 (3.18 ± 0.11 μ m; $n = 9$ axons/3 animals; $p = .0114$). In mature animals, at around P50 (P49/P53), the diameter of GBCLat (3.42 ± 0.11 μ m; $n = 6$ axons /2 animals) was comparable to the value on P25 ($p > .9999$). Hence, axon diameter in GBCLat increases markedly after hearing onset.

We observed a similar, albeit statistically insignificant, trend toward increasing axon caliber in GBCMed (Figure 6d, light blue) from

P8, with an average internodal diameter of 1.20 ± 0.07 μ m ($n = 5$ axons/2 animals), to P10 (1.55 ± 0.13 μ m, $n = 7$ axons/5 animals; $p = .436$, one-way ANOVA with Bonferroni's post-hoc test). However, the diameter of GBCMed increased significantly from P15 (1.26 ± 0.05 μ m; $n = 8$ axons/6 animals; $p = .5627$) to P17 (2.08 ± 0.08 μ m, $n = 5/2$; $p < .0001$). In contrast to GBCLat, the diameter of GBCMed did not increase significantly after this developmental stage, reaching and was 2.39 ± 0.13 μ m ($n = 8$ axons/2 animals; $p = .66841$) at P25 and 2.41 ± 0.08 μ m ($n = 6$ axons /2 animals; $p > .9999$) at \sim P50. Comparison of GBCLat with GBCMed (Figure 6e) at the time points described above showed that the diameters of the two fiber types did not differ significantly from each other at P8–P15, but had diverged strongly by P25 (P8: $p = .50$, Student's *t*-test; P10: 0.3829 , Mann–Whitney *U* test; P15: $p = .541$, *t*-test; P17: $p = .0975$,

t-test; P25: $p = .0004$, *t*-test). Moreover, this difference in axon caliber persisted into adulthood at \sim P50 ($p < .0001$, *t*-test). Therefore, the axon caliber of GBClat and GBCmed did not begin to differ until P17, but then a dramatic increase in the diameter of GBClat occurred over the following week.

Comparison of the development of axonal and nodal diameter (Figure 6f) shows that they are similar in young animals at P10/15 (GBClat: axon diameter: $1.48 \pm 0.09 \mu\text{m}$, node diameter: $1.27 \pm 0.07 \mu\text{m}$; GBCmed: axon diameter: $1.40 \pm 0.09 \mu\text{m}$, node diameter: $1.25 \pm 0.07 \mu\text{m}$). In contrast to the axon caliber (see above), the nodal diameter increases only slightly between P15 and P25 (see above).

2.6 | Delayed and differential axon diameter growth causes an unusual L/d ratio in laterally ending GBC fibers only

The developmental increase in axon diameter observed following hearing onset (in particular in the GBClat fibers) combined with the stable internode length, leads to a differential developmental reduction in the ratio of internode length to axon diameter (L/d) (Figure 6g) in GBClat only. Far from the calyx, GBClat axons in young animals (P10/15) exhibited a mean L/d ratio of $137.2 \pm 8.38 \mu\text{m}$ ($n = 18$ axons/7 animals), which fell by almost half to $69.42 \pm 5.06 \mu\text{m}$ in young adults ($n = 9$ axons/3 animals, $p < .0001$, Student's *t*-test) solely as a result of the change in axon caliber. The L/d ratio in GBCmed only showed an insignificant trend in axon caliber from animals ($139.7 \pm 13 \mu\text{m}$, $n = 15$ axons/11 animals) to young adults ($103.8 \pm 9.89 \mu\text{m}$, $n = 8$ axons/2 animals; $p = .066$ Student's *t*-test). Therefore, the increase in the axon caliber of GBClat relative to GBCmed during the initial period after hearing onset leads to a highly significant difference between the L/d ratios of the two cell types in young adults at P25 (P10/15: $p = .8648$; P25: $p = .0059$, Student's *t*-test).

Taken together, the results of our morphometrical analysis show that internode length is stable and does not differ between young animals and young adults and that the increase in axon caliber after hearing onset, particularly in GBClat, leads to the unusually low L/d ratio in low-frequency GBClat fibers. Hence, it is the late (after hearing onset) change of axon diameter that is responsible for the changing L/d -ratio, not differential myelination.

3 | DISCUSSION

Myelination patterns and axonal morphology can affect and shape the transmission of action potentials along myelinated fibers and thereby tune their conduction timing to meet specific requirements (Almeida & Lyons, 2017; Seidl et al., 2010; Seidl & Rubel, 2016). Two central factors that determine action potential velocity and fidelity are the lengths of myelin sheaths (Suminaite et al., 2019) and the axon diameter (Hodgkin, 1954; Ibrahim et al., 1995; Murray & Blakemore, 1980; Waxman, 1980). Moreover, at least for GBC axons, it is the

relationship of internode length to axon diameter (L/d ratio) that appears to be the key factor in shaping the arrival times of action potential at target nuclei (Ford et al., 2015). How myelination patterns are established, and to what extent the axon itself and/or the oligodendrocyte contribute to determining the L/d ratio are therefore crucial questions for understanding neuronal circuit adaptation of temporally precise processing.

We therefore traced the development of internode length and axon diameter in the sound localization circuit of the Mongolian gerbil, in which refined control of timing is crucial for sound localization. Here, we have shown that at GBC axons, irrespective of their frequency tuning, the internode length is set prior to the maturation of the axon diameter. Our analyses revealed that, while myelin sheath length before hearing onset already conforms to adult-like patterns, the axon diameter—in particular in low-frequency GBC axons—strongly increases after hearing onset. As a consequence, the L/d ratio decreases to unusually low values in low-frequency GBCs (Ford et al., 2015), which are required for encoding the exact arrival times of inputs at the MSO (Grothe et al., 2010). Thus, our findings show that, at least at GBC axons, it is the axon itself that retrospectively modifies the L/d ratio to accommodate its specific demands. Our data support the hypothesis that internodal length and axon caliber can be independently regulated (Kandler et al., 2009). Moreover, we were able to show that the regulation of axon diameter is an essential mechanism for the refinement of the AVCN-MNTB tract to ensure rapid action-potential conduction. Given that internode length is set early during postnatal development and at a time that precedes acoustic experience, although spontaneous activity is present (Sonntag et al., 2009), it appears that oligodendrocyte-intrinsic programs are underlying the early determination of myelin sheath length. The presence of heterogeneous oligodendrocyte populations (Bechler et al., 2015; Kessarar et al., 2006; Murtie et al., 2007; Rowitch & Kriegstein, 2010; Tripathi et al., 2010) with distinct functions (Marisca et al., 2020; Murtie et al., 2007) has been reported previously. Moreover, oligodendrocytes are able to form myelin sheaths along inert fibers in the absence of any axonal signals, and the lengths of sheaths are equivalent to in-vivo lengths (Bechler et al., 2015). Thus, oligodendrocyte-intrinsic signals based on distinct populations could indeed account for the establishment of myelination patterns at GBC axons. Since the myelin sheath lengths on GBC axons are established before the oligodendrocyte can sense the final axon diameter, we can rule out the possibility that different oligodendrocytes sense the diameter of an axon, and differentially use this information to direct the formation of sheaths in accordance with the axon diameter in low- and high-frequency fibers (Bechler et al., 2015; Hursh, 1939; Lee et al., 2002; Rushton, 1951). The fact that the increase in axon diameter occurs after hearing onset raises the question as to whether sound-evoked activity is involved in modifying the structural parameters. On the one hand, GBC axons in mice have been shown to increase in diameter after hearing onset and this increase depends on sensory activity (Sinclair et al., 2017). However, this is only the case in the direct vicinity of the calyx of Held, an area that morphologically deviates from the rest of the axon (Ford et al., 2015; Stange-Marten et al., 2017). More distant from the calyx



such an activity-dependent increase does not occur (Stancu et al, under revision). However, mice lack low-frequency hearing (Heffner & Masterton, 1980) and their GBCs do not show unusual L/d ratios (Stange-Marten et al., 2017). On the other hand, several special developments in the low-frequency ITD processing circuit have been shown to depend on early sensory activity. Inhibitory inputs at the MSO become physiologically and structurally refined in a process that has been shown to depend on acoustic experience (Kapfer et al., 2002; Magnusson et al., 2005). Coherently, proper (normal adult-like) ITD tuning requires early sensory experience (Seidl & Grothe, 2005). However, it remains to be determined whether or not acoustic experience also plays a role in differentially adjusting the diameter (and thus the L/d ratio) in low-frequency GBCs. Taken together, our findings provide direct anatomical evidence that supports the theory of a “hard-wired” myelination pattern established by intrinsic properties, which is then modified by the secondary axon thickening (Bechler et al., 2017).

Secondly, the present study provides evidence that the maturation of Nodes of Ranvier along GBC fibers correlates with the maturation of the axon diameter. We have shown that, shortly after hearing onset, most nodes display immature clusters of nodal markers, and the axon diameter has not yet matured. Node maturation continues until the 3rd and 4th postnatal week, as does that of the axon diameter. In general, we found that Nodes of Ranvier exhibit similar clusters of nodal components during development, comparable to those seen in other species and systems (Brivio et al., 2017; Rasband et al., 1999; Schafer et al., 2006; Susuki et al., 2013; Vabnick et al., 1996; Xu et al., 2017), although the general time course seems to be postponed and prolonged in the gerbil's sound-localization system. This delayed development, relative to rats and mice, also holds for eye-opening, weaning, and hearing onset (Wilkinson, 1986). Our data support the idea that, in order to form mature nodes, immature clusters consisting of nodal components first appear adjacent to the early myelin sheaths. These are termed “heminodes,” which approach each other by lateral movement of the myelin sheath and eventually fuse to form mature nodes (Brivio et al., 2017; Feinberg et al., 2010; Pedraza et al., 2001). The immature ‘phase I’ in our study possibly corresponds to the “heminode” with myelination on only one side of the node. Such a state can be observed also in adult tissue for instance in gray matter axons of the neocortex (Orthmann-Murphy et al., 2020), but, to our knowledge and observation, not in GBC axons (except the heminode after the last internode directly at the calyx). Our intermediate “phase II” would then represent the fusion phase of two “heminodes,” until the mature “phase III”—the formation of mature nodes—when adjacent “heminodes” fuse.

Finally, we have, to our knowledge, for the first time provided evidence for a sequential maturation of Nodes of Ranvier along the axons, starting from the cell soma and advancing toward the synapse, such that nodes closer to the soma are older than those close to the synaptic terminal. We found that the proportion of mature nodes is higher close to the AVCN (which includes the cell bodies of GBC axons) than it is in the vicinity of the MNTB (where the calyx of Held forms), especially at P12 and P15. This maturation timetable is

compatible with the fact that axons grow from soma to synapse (De Castro, 2003; Goldberg, 2003; Mueller, 1999). Axon-intrinsic factors that initiate node formation (Rasband & Peles, 2016) probably accumulate earlier near the cell body, since nodal scaffolding proteins such as AnkG must be transported in vesicles from the soma of neurons to the developing axon (Kaplan et al., 1997; Susuki et al., 2013).

Further studies need to reveal more details about the role of spontaneous activity before, as well as sound-driven activity after hearing onset. There is prominent spontaneous activity propagating along auditory before the onset of hearing (Sonntag et al., 2009; Tritsch et al., 2010) that is known to refine auditory brainstem circuits (Clause et al., 2014; Kim & Kandler, 2003; Kim & Kandler, 2010), and there is evidence, that such activity can influence myelination as well (Koudelka et al., 2016; Mensch et al., 2015; Mitew et al., 2018). Moreover, it remains to be seen whether the increase of axon caliber in low-frequency GBC fibers is related to the sound-driven activity.

Overall, the present study provides a more detailed description of when specific axonal and myelin characteristics are established during development. It also demonstrates—once again—that specialized circuits in the auditory brainstem in which the timing of action potentials is crucial remain a worthwhile model system in which to study general questions relating to myelination, not only because humans also use microsecond interaural time differences, like gerbils.

4 | METHODS

Mongolian gerbils (*Meriones unguiculatus*) were housed in a temperature-controlled room (23°C) with a fixed 12-h light/dark cycle. A total number of 38 animals of either sex and of specified age (P6–P53) were used for this study. All experiments were approved in accordance with the stipulations of the German Animal Welfare Law (*Tierschutzgesetz*).

4.1 | In vitro axon tracing

Animals were deeply anesthetized with pentobarbital (5 µg/g body weight) and intracardially perfused with ice-cold Ringer's solution containing heparin. Animals were decapitated and the brainstem was quickly removed from the skull under ice-cold ACSF comprising (in millimoles): 125 NaCl, 2.5 KCl, 1 MgCl₂, 2 CaCl₂, 10 glucose, 1.25 NaH₂PO₄, 26 NaHCO₃, 0.5 ascorbic acids, 3 myo-inositol, and 2 pyruvic acid (all chemicals from Sigma-Aldrich). For anterograde tracing of GBC axons, two different approaches were used. The first was carried out as described previously (Ford et al., 2015; Stange-Marten et al., 2017). For the second tracing approach, a biocytin crystal (Sigma-Aldrich, B4261) was placed on the anteroventral cochlear nucleus (AVCN) on one side of the brain. All subsequent steps were the same for both approaches. Explants were transferred to a chamber with oxygenated ACSF and incubated for 2.5–3 h at room temperature to allow for homogeneous distribution of the tracer in the

axons. The brainstems were then immersion-fixed in 4% paraformaldehyde solution for 2 h at room temperature, and stored in the fixative overnight at 4°C.

4.2 | Immunohistochemistry and confocal microscopy

Brainstems were sectioned coronally at 180 μm for axon tracing, and at 80–100 μm for node development experiments and myelin stainings, using a vibratome slicer (Leica VT 1200S). Sagittal brainstem sections were cut at 80 μm for trapezoid body (TB) fiber cross-section experiments. Sections were rinsed with PBS and transferred to a blocking solution containing 1% bovine serum albumin (0.5% bovine serum albumin for TB cross-section experiments), 0.25%–2% Triton X-100 (depending on the grade of myelination and slice thickness) and 0.1% saponin in PBS. Multiple immunofluorescence labeling was performed with the following primary antibodies: ankyrinG (AnkG; Synaptic Systems; 386–003; rabbit IgG; 1:500); L + K1.2 (NeuroMab, USA; 75–008 clone K14/16; mouse IgG2b; 1:500); myelin basic protein (MBP; ab7349, abcam; rat IgG; 1:150); contactin-associated protein1 (CASPR; NeuroMab, USA; 75–001 clone 65/35; mouse IgG1; 1:500); Neurofilament-associated protein (3A10; Development Studies Hybridoma Bank, 3a10 serum, mouse IgG1, 1:120, neurofilament heavy (NFH; ab4680; Abcam; chicken IgY; 1:300). Corresponding secondary antibodies (donkey anti-rat Alexa-488, 1:200; goat anti-mouse IgG1 Alexa-488, 1:300; donkey anti-rabbit Alexa-488, 1:200; donkey anti-rabbit Alexa-647, 1:300; donkey anti-mouse (H + L) A-647, 1:200; goat anti-mouse IgG2b Alexa-594, 1:200; donkey anti-rabbit Alexa-594, 1:200; donkey-anti-mouse Cy3, 1:400; goat anti-mouse IgG1 DyLight 405, 1:100; donkey-anti-chicken Cy3 1:200; all from Dianova), Streptavidin-Cy3 (Dianova, 1:300) and Fluorescent Neurotrace blue (Life Technologies, N21479; 1:200) were applied. Sections were mounted in Vectashield antifade medium (Vector Laboratories) under coverslips and sealed with nail polish. All antibodies used are validated by their suppliers. Confocal optical sections were acquired with a Leica TCS SP5-2 confocal laser-scanning microscope (Leica Microsystems) equipped with HCX PL APO X63/numerical aperture 1.3 glycerol 37°C objective. Fluorochromes were visualized with excitation wavelengths of 405 nm (emission filter, 410–430 nm) for Nissl Blue & DL 405, 488 nm (emission filter, 510–540 nm) for Alexa-488, 561 nm (emission filter, 565–585 nm) for tetramethylrhodamine dextran, Cy3 and Streptavidin-Cy3, 594 (emission filter 605–625 nm) for Alexa-594 or Texas Red, and 633 nm (emission filter 640–760 nm) for Alexa-647. For axon tracing experiments, overlapping stacks of images were acquired from coronal brainstem slices at the level of the trapezoid body in the area spanning the MNTB and the contralateral tracer injection site (ACVN); voxel size: 482 \times 482 \times 500 nm. For node development experiments, stacks were acquired at distinct regions along the area from the AVCN to the MNTB; voxel size: 96.29 \times 96.29 \times 293.73 nm. For myelin experiments, stacks were acquired from the left half of coronal brainstem slices in the area of the superior olivary complex. For TB cross-

section experiments, stacks were acquired from sagittal brainstem slices in the area of the trapezoid body; voxel size: 50 \times 50 \times 500 nm. Red-green-blue (RGB) stacks, montages of RGB optical sections, and maximum-intensity projections were assembled using the ImageJ 1.37 k plug-ins and Adobe Photoshop 8.0.1 (Adobe Systems) software and the Affinity Photo 2 (Serif) software. For axon tracing experiments, GBC fibers were identified by calyces of Held that terminated in the contralateral MNTB and then back tracked across sections toward the cochlear nucleus. On the basis of their exact site of termination in the MNTB, GBC axons were classified as being either medially or laterally terminating. MNTB borders were determined using a counterstain (Fluorescent Neurotrace blue).

4.3 | Morphometry

Using the Paintbrush tool, individual axons of GBCs filled with tetramethylrhodamine dextran or biocytin were manually labeled by following a single axon successively through each optical section of the confocal image stack. Subsequently, the neighboring axons were digitally deleted. The same axon was identified in the neighboring overlapping confocal image stacks and digitally extracted. Nodes of Ranvier were identified based on immunohistochemical labeling (IHC) of nodal and paranodal or juxtaparanodal marker proteins (AnkG and CASPR or $K_v1.2$). Distances between Nodes of Ranvier (measured mid-node to mid-node) were measured in three dimensions in confocal image stacks using the ImageJ 1.37 k Sync Measure three-dimensional tool. Internodal axon diameter and nodal diameter measurements were assessed in two dimensions from maximum-intensity projections of confocal image stacks. Axon diameter was assessed by multiple measurements of internodal axon segments of intracellularly labeled axons in between immunostained Nodes of Ranvier, and the average diameter per axon across several measurements was used for analysis.

4.4 | Electron microscopy

Two gerbils aged P10 were deeply anesthetized with pentobarbital (5 $\mu\text{g}/\text{g}$ body weight) and intracardially perfused with Ringer's solution followed by perfusion with 2.5% glutaraldehyde plus 2% PFA in 0.075 M cacodylate buffer (CB). Brainstems were removed from the skull and post-fixed in the same fixative overnight at 4°C. Brainstems were washed in CB and sectioned parasagittally at 500 μm using a vibratome slicer and a 1 mm \times 1 mm block containing the trapezoid body fibers was extracted using a razor blade. Tissue was washed in CB and post-fixed in 1% OsO_4 in 0.1 M CB for 1–2 h. After washing and dehydrating in a graded series of acetone, tissue was embedded in resin, and ultrathin sections were cut. The sections were mounted on formvar coated copper grids, contrasted with lead citrate and uranyl acetate, and photographed with an FEI Morgagni transmission electron microscope at 80 kV.



4.5 | Statistics

Data were analyzed using GraphPad Prism8 (GraphPad Software, La Jolla, CA), IgorPro 5.02 (Wavemetrics), and MS Excel 2021 (Microsoft, Redmond, WA). Data are represented as mean \pm SEM. Tests for normal distribution were performed using the Kolmogorov–Smirnov test. p Values were derived from two-sided Student's t -tests, or one-way ANOVA with Tukey's post-hoc test, provided the dataset passed the normality test. Otherwise, significance was tested using either the Mann–Whitney U test or the Kruskal–Wallis test with Dunn's post-hoc test (p values are significant if they are less than 0.05). p Values in Figures 5b and 6c derive from χ^2 tests. Data presented in Figure 4a,c were fit with exponential functions. No blinding was done for data analysis of axon diameter, node diameter, and internode length, simply because one cannot measure the length of single labeled axons without starting at the region of termination in the MNTB. However, measuring persons were ignorant of the details of the ITD circuit and, hence, the conceptual issues of the study. Quantitatively identical measurements were used for the analysis of all data.

AUTHOR CONTRIBUTIONS

Alisha L. Nabel, Laurin Teich, Michael Pecka, and Benedikt Grothe conceived the study and Alisha L. Nabel, Laurin Teich, Hilde Wohlfrom, and Olga Alexandrova designed the experiments. Alisha L. Nabel, Laurin Teich, Hilde Wohlfrom, Olga Alexandrova, Martin Heß performed research; Alisha L. Nabel, Laurin Teich, Olga Alexandrova, Martin Heß analyzed data. Alisha L. Nabel, Laurin Teich prepared figures and wrote the manuscript with supervision from B.G.; Michael Pecka and Benedikt Grothe jointly supervised this work; All authors provided comments and approved the manuscript.

ACKNOWLEDGMENTS

The authors thank Paula Gundi, Annalena Malzacher, and Sina Bleis for their help in immunostainings, blind analysis of the data and valuable discussion. This study was supported by the Deutsche Forschungsgemeinschaft DFG (SFB 870, project B02 to Michael Pecka and Benedikt Grothe) and by the Munich Cluster for Systems Neurology (Synergy). The 3A10 antibody was obtained from the Developmental Studies Hybridoma Bank. The microscopic images were taken at the center for advanced light microscopy (CALM) at the LMU Munich. We thank L. Dimou, T. Czopka and P. Hardy for valuable comments on earlier versions of the manuscript. Open Access funding enabled and organized by Projekt DEAL.

FUNDING INFORMATION

Deutsche Forschungsgemeinschaft DFG (SFB 870, project B02 to Michael Pecka and Benedikt Grothe), Munich Cluster for Systems Neurology (SyNergy Tandem Project B7).

CONFLICT OF INTEREST STATEMENT

The authors declare no competing interests.

DATA AVAILABILITY STATEMENT

The data used during the study are available from the corresponding author on reasonable request.

ORCID

Laurin Teich <https://orcid.org/0009-0003-9281-2056>

Martin Heß <https://orcid.org/0000-0002-7751-9711>

Michael Pecka <https://orcid.org/0000-0001-8960-1651>

Benedikt Grothe <https://orcid.org/0000-0001-7317-0615>

REFERENCES

- Almeida, D. M., & Lyons, D. A. (2017). On myelinated axon plasticity and neuronal circuit formation and function. *Journal of Neuroscience*, 37, 10023–10034.
- Arancibia-Cárcamo, I. L., Ford, M. C., Cossell, L., Ishida, K., Tohyama, K., & Attwell, D. (2017). Node of Ranvier length as a potential regulator of myelinated axon conduction speed. *eLife*, 6, e23329.
- Bechler, M. E., Byrne, L., & ffrench-Constant, C. (2015). CNS myelin sheath lengths are an intrinsic property of oligodendrocytes. *Current Biology*, 25, 2411–2416.
- Bechler, M. E., Swire, M., & ffrench-Constant, C. (2017). Intrinsic and adaptive myelination—A sequential mechanism for smart wiring in the brain. *Developmental Neurobiology*, 78, 68–79.
- Brand, A., Behrend, O., Marquardt, T., McAlpine, D., & Grothe, B. (2002). Precise inhibition is essential for microsecond interaural time difference coding. *Nature*, 417, 543–547.
- Brivio, V., Favre-Sarrailh, C., Peles, E., Sherman, D. L., & Brophy, P. J. (2017). Assembly of CNS nodes of Ranvier in myelinated nerves is promoted by the axon cytoskeleton. *Current Biology*, 27, 1068–1073.
- Clause, A., Kim, G., Sonntag, M., Weisz, K. J. C., Vetter, D. E., Rübsamen, R., & Kandler, K. (2014). The precise temporal pattern of prehearing spontaneous activity is necessary for tonotopic map refinement. *Neuron*, 82, 822–835.
- De Castro, F. (2003). Chemotropic molecules: Guides for axonal pathfinding and cell migration during CNS development. *News in Physiological Sciences*, 18, 130–136.
- Feinberg, K., Eshed-Eisenbach, Y., Frechter, S., Amor, V., Salomon, D., Sabanay, H., Dupree, J. L., Grumet, M., Brophy, P. J., Shrager, P., & Peles, E. (2010). A glial signal consisting of gliomedin and NrCAM clusters axonal Na⁺ channels during the formation of nodes of Ranvier. *Neuron*, 65, 490–502.
- Ford, M. C., Alexandrova, O., Cossell, L., Stange-Marten, A., Sinclair, J., Kopp-Scheinflug, C., Pecka, M., Attwell, D., & Grothe, B. (2015). Tuning of Ranvier node and internode properties in myelinated axons to adjust action potential timing. *Nature Communications*, 6, 1–14.
- Friauf, E., & Ostwald, J. (1988). Divergent projections of physiologically characterized rat ventral cochlear nucleus neurons as shown by intra-axonal injection of horseradish peroxidase. *Experimental Brain Research*, 73(2), 263–283. <https://doi.org/10.1007/BF00248219>
- Goldberg, J. L. (2003). How does an axon grow? *Genes and Development*, 17, 941–958.
- Grothe, B. (2003). New roles for synaptic inhibition in sound localization. *Nature Reviews Neuroscience*, 4, 540–550.
- Grothe, B., & Pecka, M. (2014). The natural history of sound localization in mammals – a story of neuronal inhibition. *Frontiers in Neural Circuits*, 8, 116.
- Grothe, B., Pecka, M., & McAlpine, D. (2010). Mechanisms of sound localization in mammals. *Physiological Reviews*, 90, 983–1012.
- Heffner, H. E., & Masterton, B. (1980). Hearing in glires: Domestic rabbit, cotton rat, feral house mouse, and kangaroo rat. *Journal of the Acoustical Society of America*, 68, 1584–1599. <https://doi.org/10.1121/1.385213>

- Hodgkin, A. L. (1954). A note on conduction velocity. *Journal of Physiology*, 125(1), 221–224. <https://doi.org/10.1113/jphysiol.1954.sp005152>
- Hursh, J. B. (1939). Velocity and diameter. *American Journal of Physiology*, 127, 131–139.
- Huxley, A. F., & Stampfli, R. (1949). Evidence for saltatory conduction in. *The Journal of Physiology*, 108, 315–339.
- Ibrahim, M., Butt, A. M., & Berry, M. (1995). Relationship between myelin sheath diameter and internodal length in axons of the anterior medullary velum of the adult rat. *Journal of Neurological Sciences*, 133, 119–127.
- Kandler, K., Clause, A., & Noh, J. (2009). Tonotopic reorganization of developing auditory brainstem circuits. *Nature Neuroscience*, 12, 711–717.
- Kapfer, C., Seidl, A. H., Schweizer, H., & Grothe, B. (2002). Experience-dependent refinement of inhibitory inputs to auditory coincidence-detector neurons. *Nature Neuroscience*, 5, 247–253.
- Kaplan, M. R., Meyer-Franke, A., Lambert, S., Bennett, V., Duncan, I. D., Levinson, S. R., & Barres, B. A. (1997). Induction of sodium channel clustering by oligodendrocytes. *Nature*, 386, 724–728.
- Kessaris, N., Fogarty, M., Iannarelli, P., Grist, M., Wegner, M., & Richardson, W. D. (2006). Competing waves of oligodendrocytes in the forebrain and postnatal elimination of an embryonic lineage. *Nature Neuroscience*, 9, 173–217.
- Kim, G., & Kandler, K. (2003). Elimination and strengthening of glycinergic/GABAergic connections during tonotopic map formation. *Nature Neuroscience*, 6, 282–290.
- Kim, G., & Kandler, K. (2010). Synaptic changes underlying the strengthening of GABA/ glycinergic connections in the developing lateral superior olive. *Neuroscience*, 171, 924–933.
- Koudelka, S., Voas, M. G., Almeida, R. G., Baraban, M., Soetaert, J., Meyer, M. P., Talbot, W. S., & Lyons, D. A. (2016). Individual neuronal subtypes exhibit diversity in CNS myelination mediated by synaptic vesicle release. *Current Biology*, 26, 1447–1455.
- Lee, S., Leach, M. L., Redmond, S. A., Chong, S. Y. C., Mellon, S. H., Tuck, S. J., Feng, Z.-Q., Corey, J. M., & Chan, J. R. (2002). A culture system to study oligodendrocyte myelination- processes using engineered nanofibers. *Nature Methods*, 9, 917–922.
- Lesica, N. A., Lingner, A., & Grothe, B. (2010). Population coding of interaural time differences in gerbils and barn owls. *The Journal of Neuroscience*, 30(35), 11696–11702. <https://doi.org/10.1523/JNEUROSCI.0846-10.2010>
- Magnusson, A. K., Kapfer, C., Grothe, B., & Koch, U. (2005). Maturation of glycinergic inhibition in the gerbil medial superior olive after hearing onset. *Journal of Physiology*, 568, 497–512.
- Mansour, Y., & Kulesza, R. (2021). Distribution of glutamatergic and glycinergic inputs onto human auditory coincidence detector neurons. *Neuroscience*, 468, 75–87.
- Marisca, R., Hoche, T., Agirre, E., Hoodless, L. J., Barkey, W., Auer, F., Castelo-Branco, G., & Czopka, T. (2020). Functionally distinct subgroups of oligodendrocyte precursor cells integrate neural activity and execute myelin formation. *Nature Neuroscience*, 23, 363–374.
- Mathis, S., & Vallat, J.-M. (2019). The journal behind the nodes of Ranvier? *The Lancet Neurology*, 18, 628. [https://doi.org/10.1016/S1474-4422\(19\)30203-0](https://doi.org/10.1016/S1474-4422(19)30203-0)
- Mensch, S., Baraban, M., Almeida, R., Czopka, T., Ausborn, J., El Manira, A., & Lyons, D. A. (2015). Synaptic vesicle release regulates the number of myelin sheaths made by individual oligodendrocytes in vivo. *Nature Neuroscience*, 18, 628–630.
- Mitew, S., Gobijs, I., Fenlon, L. R., McDougall, S. J., Hawkes, D., Xing, Y. L., Bujalka, H., Gundlach, A. L., Richards, L. J., Kilpatrick, T. J., Merson, T. D., & Emery, B. (2018). Pharmacogenetic stimulation of neuronal activity increases myelination in an axon-specific manner. *Nature Communications*, 9, 1–16.
- Mueller, B. K. (1999). Growth cone guidance: First steps towards a deeper understanding. *Annual Review of Neuroscience*, 22, 351–388.
- Murray, J. A., & Blakemore, W. F. (1980). The relationship between internodal length and fibre diameter in the spinal cord of the rat. *Journal of Neurological Sciences*, 45, 29–41.
- Murtie, J. C., Macklin, W. B., & Corfas, G. (2007). Morphometric analysis of oligodendrocytes in the adult mouse frontal cortex. *Journal of Neuroscience Research*, 85, 2080–2086.
- Orthmann-Murphy, J., Call, C. L., Molina-Castro, G. C., Hsieh, Y. C., Rasband, M. N., Calabresi, P. A., & Bergles, D. E. (2020). Remyelination alters the pattern of myelin in the cerebral cortex. *eLife*, 9, e56621. <https://doi.org/10.7554/eLife.56621>
- Pedraza, L., Huang, J. K., & Colman, D. R. (2001). Organizing principles of the axoglial apparatus. *Neuron*, 30, 335–344.
- Rasband, M. N., & Peles, E. (2016). The nodes of Ranvier: Molecular assembly and maintenance. *Cold Spring Harbor Perspectives in Biology*, 8, 1–15.
- Rasband, M. N., Peles, E., Trimmer, J. S., Levinson, S. R., Lux, S. E., & Shrager, P. (1999). Dependence of nodal sodium channel clustering on paranodal axoglial contact in the developing CNS. *Journal of Neuroscience*, 19, 7516–7528.
- Rowitch, D. H., & Kriegstein, A. R. (2010). Developmental genetics of vertebrate glial-cell specification. *Nature*, 468, 214–222.
- Rushton, W. A. H. (1951). A theory of the effects of fibre size in medullated nerve. *Journal of Physiology*, 115, 101–122.
- Schafer, D. P., Custer, A. W., Shrager, P., & Rasband, M. N. (2006). Early events in node of Ranvier formation during myelination and remyelination in the PNS. *Neuron Glia Biology*, 2, 69–79.
- Seidl, A. H. (2014). Regulation of conduction time along axons. *Neuroscience*, 276, 126–134.
- Seidl, A. H., & Grothe, B. (2005). Development of sound localization mechanisms in mammals is shaped by early acoustic experience. *Journal of Neurophysiology*, 94, 1028–1036.
- Seidl, A. H., & Rubel, E. W. (2016). Systematic and differential myelination of axon collaterals in the mammalian auditory brainstem. *Glia*, 64, 487–494.
- Seidl, A. H., Rubel, E. W., & Harris, D. M. (2010). Mechanisms for adjusting interaural time differences to achieve binaural coincidence detection. *Journal of Neuroscience*, 30, 70–80.
- Sinclair, J. L., Fischl, M. J., Alexandrova, O., Heß, M., Grothe, B., Leibold, C., & Kopp-Scheinflug, C. (2017). Sound-evoked activity influences myelination of brainstem axons in the trapezoid body. *Journal of Neuroscience*, 37, 8239–8255.
- Smith, R. S., & Koles, Z. J. (1970). Myelinated nerve fibers: Computed effect of myelin thickness on conduction velocity. *American Journal of Physiology*, 219, 1256–1258.
- Sonntag, M., Englitz, B., Kopp-Scheinflug, C., & Rübsamen, R. (2009). Early postnatal development of spontaneous and acoustically evoked discharge activity of principal cells of the medial nucleus of the trapezoid body: An in vivo study in mice. *Journal of Neuroscience*, 29, 9510–9520.
- Stange-Marten, A., Nabel, A. L., Sinclair, J. L., Fischl, M., Alexandrova, O., Wohlfrom, H., Kopp-Scheinflug, C., Pecka, M., & Grothe, B. (2017). Input timing for spatial processing is precisely tuned via constant synaptic delays and myelination patterns in the auditory brainstem. *Proceedings of the National Academy of Sciences of the United States of America*, 114(24), E4851–E4858. <https://doi.org/10.1073/pnas.1702290114>
- Suminaite, D., Lyons, D. A., & Livesey, M. R. (2019). Myelinated axon physiology and regulation of neural circuit function. *Glia*, 67, 2050–2062.
- Susuki, K., Chang, K. J., Zollinger, D. R., Liu, Y., Ogawa, Y., Eshed-Eisenbach, Y., Dours-Zimmermann, M. T., Osés-Prieto, J. A., Burlingame, A. L., Seidenbecher, C. I., Zimmermann, D. R., Oohashi, T., Peles, E., & Rasband, M. N. (2013). Three mechanisms assemble central nervous system nodes of ranvier. *Neuron*, 78, 469–482.
- Tolnai, S., Beutelmann, R., & Klump, G. M. (2017). Exploring binaural hearing in gerbils (*Meriones unguiculatus*) using virtual headphones. *PLoS One*, 12(4), e0175142. <https://doi.org/10.1371/journal.pone.0175142>



- Tripathi, V., Ellis, J. D., Shen, Z., Song, D. Y., Pan, Q., Watt, A. T., Freier, S. M., Bennett, C. F., Sharma, A., Bubulya, P. A., Blencowe, B. J., Prasanth, S. G., & Prasanth, K. V. (2010). The nuclear-retained noncoding RNA MALAT1 regulates alternative splicing by modulating SR splicing factor phosphorylation. *Molecular Cell*, *39*, 925–938.
- Tritsch, N. X., Rodríguez-Contreras, A., Crins, T. T. H., Wang, H. C., Borst, J. G. G., & Bergles, D. E. (2010). Calcium action potentials in hair cells pattern auditory neuron activity before hearing onset. *Nature Neuroscience*, *13*, 1050–1052.
- Vabnick, I., Novaković, S. D., Levinson, S. R., Schachner, M., & Shrager, P. (1996). The clustering of axonal sodium channels during development of the peripheral nervous system. *Journal of Neuroscience*, *16*, 4914–4922.
- Waxman, S. G. (1980). Determinants of conduction velocity in myelinated nerve fibers. *Muscle & Nerve*, *3*(2), 141–150.
- Wilkinson, F. (1986). Eye and brain growth in the Mongolian gerbil (*Meriones unguiculatus*). *Behavioural Brain Research*, *19*, 59–69.

- Xu, J., Berret, E., & Kim, J. H. (2017). Activity-dependent formation and location of voltage-gated sodium channel clusters at a CNS nerve terminal during postnatal development. *Journal of Neurophysiology*, *117*, 582–593.

SUPPORTING INFORMATION

Additional supporting information can be found online in the Supporting Information section at the end of this article.

How to cite this article: Nabel, A. L., Teich, L., Wohlfrom, H., Alexandrova, O., Heß, M., Pecka, M., & Grothe, B. (2024). Development of myelination and axon diameter for fast and precise action potential conductance. *Glia*, *72*(4), 794–808. <https://doi.org/10.1002/glia.24504>